Textile & Leather Review

ISSN 2623-6281 | www.tlr-journal.com | 10.31881/TLR

A GNSS-PWV-Assisted Hybrid Vertical Layering Method for Improving Short-Term Precipitation Forecasts in the WRF Model

Ruikun Wang

How to cite: Wang R. A GNSS-PWV-Assisted Hybrid Vertical Layering Method for Improving Short-Term Precipitation Forecasts in the WRF Model. Textile & Leather Review. 2026; 9:2843-2869. https://doi.org/10.31881/TLR.2026.2843

How to link: https://doi.org/10.31881/TLR.2026.2843

Published: 25 April 2026

A GNSS-PWV-Assisted Hybrid Vertical Layering Method for Improving Short-Term Precipitation Forecasts in the WRF Model

Ruikun Wang

College of Geomatics, Xi'an University of Science and Technology, Xi'an 710054, Shaanxi, China
13659258522@163.com

Article
https://doi.org/10.31881/TLR.2026.2843
Published 25 April 2026

ABSTRACT

Accurate atmospheric water vapor information is crucial for improving the performance of numerical weather prediction (NWP) models. However, current models are limited by insufficient vertical layering structures that fail to capture the spatial variability of water vapor, as well as outdated and low-resolution underlying surface data. To address these issues, this study proposes a hybrid vertical layering method that integrates Global Navigation Satellite System (GNSS)-derived precipitable water vapor (PWV) to enhance short-term precipitation forecasting. The method introduces a vertically weighted water vapor equalization principle and uses spatially continuous water vapor data to adaptively optimize the vertical structure within the key precipitation height range (1–7 km). In addition, high-resolution (30 m) land cover data from the 2020 global dataset are used to replace the default USGS data in the WRF model. Xi'an and surrounding areas are selected as the study region to evaluate the impacts of surface data updating and vertical layering optimization. Results show that the combined approach improves 1-hour precipitation forecasts, reducing RMSE, MAE, and bias by 15.2%, 12.5%, and 55.2%, respectively, with the correlation coefficient increasing to 0.53. Significant improvements are also observed in temperature, pressure, and relative humidity, demonstrating enhanced forecasting capability.

KEYWORDS

GNSS, precipitable water vapor, WRF model, hybrid vertical layering, precipitation forecasting

INTRODUCTION

The spatial resolution of numerical weather prediction (NWP) models is jointly determined by horizontal grid spacing and vertical layer spacing, which together define the smallest-scale atmospheric processes that can be effectively resolved by the model [1]. In recent years, driven by the integration of multi-source observational data and continuous improvements in atmospheric reanalysis products, the horizontal resolution of regional

NWP models has progressively reached convection-permitting scales, leading to substantial improvements in short-term weather simulation and forecasting capabilities [2]. Nevertheless, accurately simulating and forecasting extreme weather events, such as heavy rainfall and severe convection, remains a major challenge [3,4].

A growing body of research indicates that the vertical resolution of NWP models, in coordination with horizontal resolution, plays a critical role in the simulation of convective processes [5]. Enhancing vertical resolution enables a more detailed representation of the three-dimensional thermodynamic and dynamic structures of the atmosphere, thereby improving the depiction of mesoscale weather mechanisms and overall model performance. Persson (1991) pointed out that inconsistencies between horizontal and vertical resolutions may induce spurious gravity waves, thereby increasing simulation errors [6]. Du et al. (2021) demonstrated that increasing vertical resolution enhances the warm-core structure and improves the simulation of asymmetric wind fields, leading to more accurate predictions of typhoon intensity and track [7]. Yang et al. (2016) showed that increasing vertical resolution in the WRF model significantly improves the simulation of sea fog over the Yellow Sea [8]. Khansalari et al. (2021) further confirmed, through sensitivity experiments, that appropriate vertical layering is crucial for improving precipitation forecast accuracy [9]. Yin et al. (2018) improved heavy precipitation simulations in southern China by increasing the number of vertical levels below 850 hPa and above 200 hPa in the WRF model [10]. Wu et al. (2019) found that higher vertical resolution improves the simulation of typhoon intensity, while Shao et al. (2020) reported enhanced short-term precipitation forecasting performance with refined vertical resolution during winter over the continental United States [11,12]. Despite these advances, most existing approaches focus primarily on increasing the number of vertical layers, while paying less attention to how the layers are distributed. The limitation of traditional terrain-following coordinates extends beyond insufficient vertical resolution. The fixed layer distribution lacks adaptability to the highly variable vertical structure of atmospheric water vapor, particularly under convective conditions. A fixed vertical structure may therefore fail to adequately resolve these key layers, leading to inaccuracies in representing moisture-related processes that are critical for precipitation formation.

On the other hand, improvements in the spatial resolution of NWP models are con-strained by the resolution and quality of static geographical data [13]. Land cover change, closely associated with climate evolution, ecological processes, and human activities, is a key factor influencing the Earth system. As a comprehensive representation of surface material types and their properties, land cover effectively reflects land-use changes

driven by anthropogenic activities. In NWP models, complex interactions and feedback mechanisms exist between land surface processes and atmospheric physics, among which underlying surface data serve as fundamental inputs. Significant changes in land surface structure and spatial distribution, particularly under rapid urbanization, play an important role in modulating convective weather processes.

Recent studies have highlighted the importance of high-quality land surface data. Karakani et al. (2024) demonstrated that the accuracy of static surface data significantly affects the spatial distribution of simulated temperature [14]. Jee et al. (2016) showed that high-resolution land surface data can substantially improve the simulation accuracy of meteorological variables in megacities [15]. Yan et al. (2021) systematically analyzed the uncertainties in temperature and precipitation simulations arising from different land surface models and land-use datasets, revealing that their impacts are significant and interdependent, particularly for precipitation [16]. Schicker et al. (2016) compared USGS, MODIS, and CORINE land-use datasets and found that higher-resolution and more up-to-date CORINE data better represent surface characteristics and improve simulations of land surface temperature and other meteorological variables [17].

In summary, numerous studies have demonstrated that optimizing vertical resolution and layering structures, as well as incorporating high-quality, high-resolution, and up-to-date land surface data, is essential for improving NWP model performance, particularly in precipitation forecasting. However, limited attention has been given to the use of GNSS-derived tropospheric products for improving the initial vertical layering of NWP models, especially in combination with high-quality land surface data. Therefore, to further enhance precipitation forecasting accuracy, it is necessary to jointly consider the effects of complex regional geographical conditions and the vertical distribution of atmospheric water vapor, thereby improving the capability of NWP models in simulating precipitation processes.

EXPERIMENTAL

Materials and Methods

Overview of the Study Area

This study focuses on Xi'an and its surrounding regions, located within the coordinates of 107°40′–109°49′ E and 33°42′–34°45′ N, with an east–west extent of 204 km and a north–south span of 116 km. The study area is situated in the central Guanzhong Plain of the middle reaches of the Yellow River Basin in northwestern China. Its topography and climate form a coupled and co-evolving natural geographical system.

Climatically, it belongs to a warm temperate semi-humid continental monsoon regime. The Qinling Mountains exert a strong influence on regional climate through orographic blocking and lifting effects, resulting in concentrated precipitation in the piedmont areas and the formation of distinct vertical climatic zones.

Seasonal variations are pronounced, with clear alternations between cold/warm and dry/wet conditions. Winters are typically cold, with weak winds, frequent haze, and limited precipitation. Springs are warm, dry, and windy, with highly variable weather. Summers are hot and humid, characterized by abundant rainfall, occasional drought periods, and frequent thunderstorms and strong winds. Autumns are cool, with rapidly de-creasing temperatures and persistent rainfall events.

Based on these characteristics, Xi'an and its surrounding regions were selected as the study area, with particular emphasis on Xi'an city. The WRF model is configured using a three-level nested domain with a nesting ratio of 1:3. The outermost domain (D01), with a spatial resolution of 9 km, covers parts of Shaanxi and Shanxi Provinces. The intermediate domain (D02) has a resolution of 3 km and encompasses central Shaanxi and adjacent areas. The innermost domain (D03), with a resolution of 1 km, focuses on Xi'an and its surrounding regions. The geographical location of the study area and the spatial distribution of observation stations are shown in Figure 1.

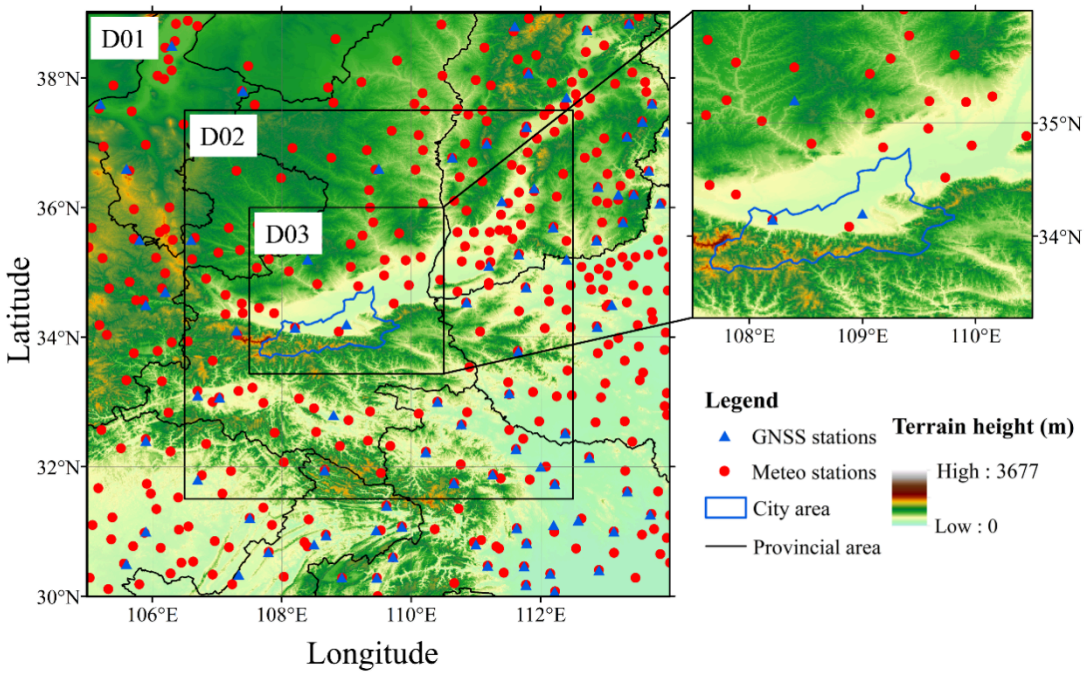

Figure 1. Geographical distribution of GNSS and Met stations in Xi'an and its surrounding areas

Data Sources

(1) Land Surface Data

The GLC_FCS_30D dataset is the first global dynamic land cover product at 30 m spatial resolution derived using a continuous change detection approach. It adopts a detailed classification scheme comprising 35 land cover types and spans the period from 1985 to 2022. Prior to 2000, the dataset was updated at five-year intervals, whereas annual up-dates have been available since 2000. Specifically, the dataset was developed by integrating a continuous change detection method, a locally adaptive updating model, and spatiotemporal optimization algorithms based on dense time-series Landsat imagery. Validation results indicate that the overall accuracy of the basic classification system (10 primary land cover types) reaches 80.88% (±0.27%), while the overall accuracy based on the Level-1 Land Cover Classification System (LCCS) scheme (17 classes) is 73.24% (±0.30%) [18].

(2) Meteorological Observations

Meteorological variables are key factors governing the occurrence of precipitation, and their relationships with precipitation processes are highly nonlinear and complex. Surface temperature, as a core variable representing land–atmosphere interactions, directly regulates the energy flux and balance between the land surface and the atmosphere. In addition, the distribution and variation of atmospheric pressure influence vertical air motion, thereby playing a crucial dynamical role in the formation and development of precipitation. Relative humidity reflects the saturation level of atmospheric water vapor and serves as a fundamental physical condition affecting cloud microphysical processes and precipitation efficiency. These factors collectively contribute to precipitation through a multiscale and multi-factor interaction mechanism [19]. Accordingly, this study evaluates the accuracy of four key meteorological variables: surface temperature, atmospheric pressure, relative humidity, and precipitation. Observational data from 42 meteorological stations within the study area, provided by the China Meteorological Administration (CMA), are used for validation.

(3) WRF Forcing Data

The Weather Research and Forecasting (WRF) model in this study is driven by Global Forecast System (GFS) data, which provide global numerical weather prediction outputs at a spatial resolution of approximately 0.25° × 0.25° [20]. The GFS system performs data assimilation and forecasting four times daily at 00, 06, 12, and 18 UTC, with forecast products extending up to 16 days.

The GFS dataset consists of 127 vertical layers, extending from the ground all the way up to the 0.01 hPa altitude in the stratosphere, and can provide a detailed description of the atmospheric conditions at each layer. It provides a wide range of atmospheric and land surface variables, including temperature, precipitation, soil moisture, and atmospheric ozone concentration, thereby supplying essential initial water vapor and meteorological conditions for the numerical model [21].

In this study, a short-term precipitation event that occurred in Xi'an from 21 to 25 April 2021 is selected as the simulation period.

GNSS-PWV-Assisted Hybrid Vertical Layering Method

Precipitation, as a fundamental output of atmospheric processes, exhibits significant variability in both intensity and spatial distribution due to the combined influences of meteorological conditions and geographical factors. This variability is highly complex in both temporal and spatial dimensions. To address the limitations of the conventional WRF model—namely, the low quality and outdated nature of underlying surface data, as well as the inability of traditional vertical layering schemes to adequately represent the spatial variability of atmospheric water vapor—this study proposes a GNSS-PWV-assisted hybrid vertical layering method.

The proposed approach integrates high-quality, high-resolution land surface data with a water-vapor-informed vertical layering scheme. First, high-resolution land use data (30 m) for 2020 are obtained from a global land cover dataset. These data are then processed into a format compatible with the WRF model and used to replace the default underlying surface data. Next, corrected GFS-derived precipitable water vapor (PWV) data are incorporated. Based on a water-vapor-weighted vertical equalization principle, the vertical layer distribution within the key precipitation height range of the WRF model is adaptively redefined.

Finally, the reconstructed high-resolution land surface data and the optimized hybrid vertical layering structure are incorporated into the WRF model for numerical weather forecasting. The overall workflow of the proposed method is illustrated in Figure 2.

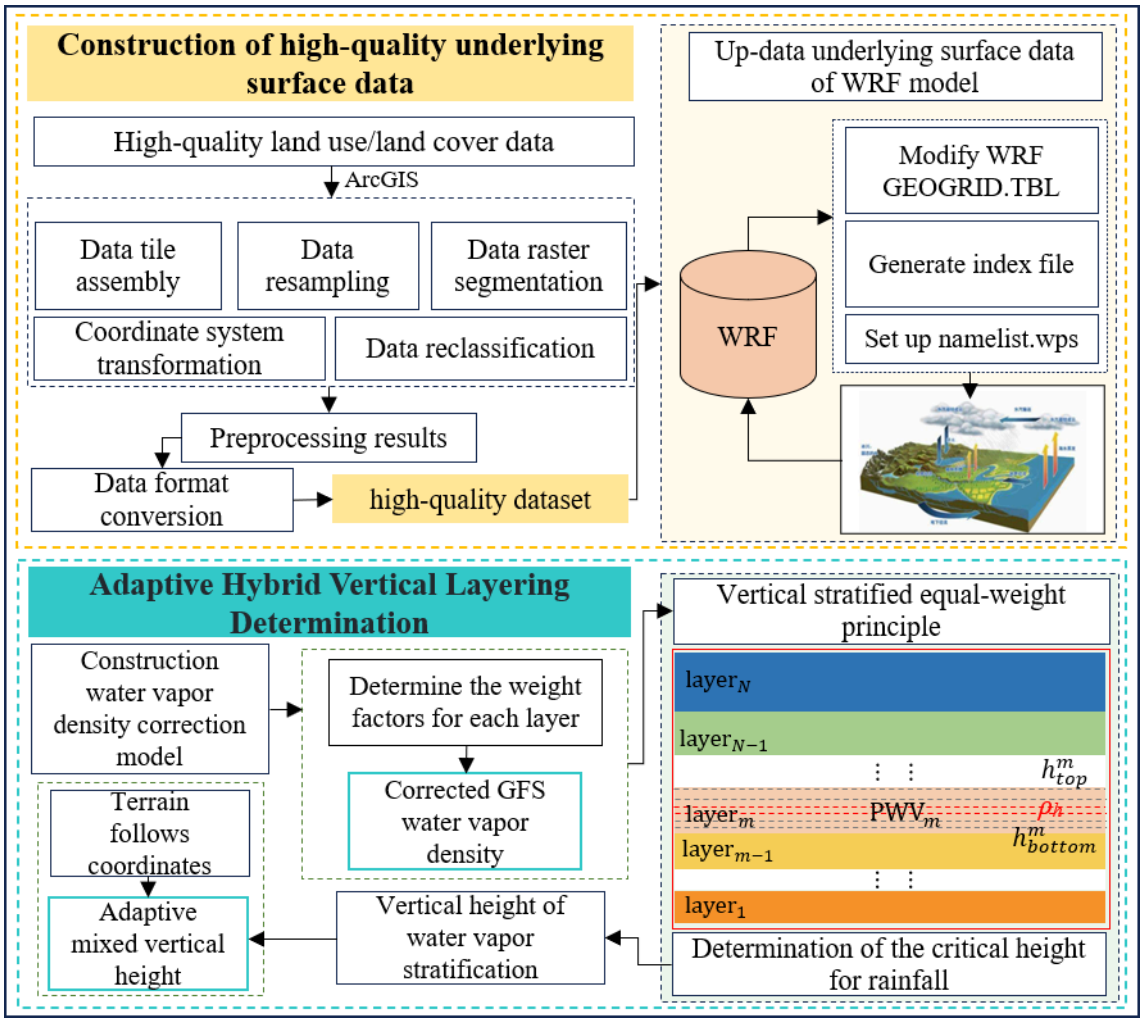

Figure 2. Flowchart of the Hybrid Vertical Layering Method for GNSS Water Vapor Assisted Numerical Model

(1) Hybrid Vertical Layering Scheme

Terrain-following (TF) coordinates are the primary approach used in the WRF model to define the vertical layer structure [22]. However, this method has limitations in effectively representing the spatial variability of water vapor, which can adversely affect the accuracy of precipitation forecasts [23]. To address this issue, the method proposed in this study introduces a vertically stratified, water vapor–equal-weighting principle to redefine the vertical levels within the key precipitation-related altitude range (1–7 km) in the WRF model [24]. Figure 3 illustrates a schematic diagram of the hybrid vertical layering approach applied to this critical height range.

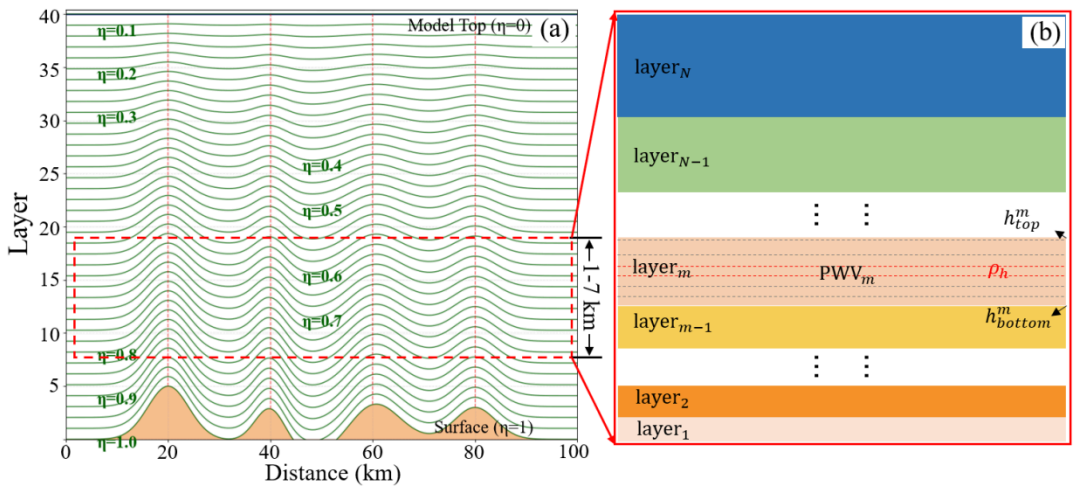

Figure 3. A schematic diagram of vertical re-layering within the key height range of the numerical weather forecasting model

(a) Acquisition of GFS water vapor density: According to the official documentation of the GFS dataset, GFS forecast data are read and the water vapor density information is extracted from multiple forecast variables.

(b) Construction of the GFS water vapor density correction model: Using the PWV residuals between the corrected GFS PWV and the uncorrected GFS PWV at arbitrary grid points for each epoch obtained in the previous step, a GFS water vapor density correction model is established. The specific formulation is given as follows:

$$\Delta PWV_{GFS}^{grid} = \sum \omega \cdot \Delta\rho_{unit} \cdot d = (\omega_1 \cdot d_1 + \omega_2 \cdot d_2 + \cdots + \omega_i \cdot d_i + \cdots + \omega_m \cdot d_m) \cdot \Delta\rho_{unit} \quad (1)$$

where ΔPWV_{GFS}^{grid} indicates the PWV residual between calibrated and uncalibrated GFS-provided PWV at each grid point; $\Delta\rho_{unit}$ represents the unit change index of water vapor density (WVD); ω_i and d_i denote the weighting and thickness in ith layer, respectively. Here, the layer is determined according to the TFM.

(c) Determination of layer-wise weights in the correction model: The weight assigned to each layer is strongly correlated with the water vapor density, reflecting its contribution to the total PWV. The specific calculation formula is as follows:

$$\omega_i = \frac{\rho_i^{GFS}}{\sum \rho_i^{GFS}} \quad (2)$$

where ρ_i^{GFS} represents the GFS-provided WVD before calibration.

(d) Acquisition of corrected GFS water vapor density: After determining the weight of water vapor density for each layer, the unit variation index of water vapor density at any grid point can be obtained. Accordingly, the corrected GFS water vapor density at each layer and grid point is calculated.

$$\rho_{GFS_i}^{cal.} = \rho_{GFS_i}^{uncal.} + \omega_i \cdot \Delta\rho_{unit} \tag{3}$$

where $\rho_{GFS_i}^{uncal.}$ and $\rho_{GFS_i}^{cal.}$ represent the uncalibrated and calibrated GFS-provided WVD, respectively.

(e) Derivation of water vapor density at different height levels: The corrected GFS water vapor density obtained in the previous steps is interpolated to derive the mean water vapor density at specific heights within the key altitude range for numerical precipitation forecasting (e.g., at 10 m intervals). The calculation formula for the water vapor density at each layer center is given as follows:

$$\rho'_{h_m} = \frac{\sum_{h=h_m}^{h_m+\Delta h} \rho_h}{2} \tag{4}$$

where ρ'_{h_m} represents the WVD at the central point of the mth layer; ρ_h denotes the averaged WVD interpolated from calibrated GFS-provided WVD; m corresponds to the mth layer within the key height range of the NWP model, spanning a height interval of ; $[h_m, h_m + \Delta h]$ is the vertical resolution, set to 10 m in this study.

f Determination of vertical layer thickness: Based on the equal-weighting principle of vertical stratification, the vertical thickness of each layer is adaptively determined using the corrected GFS PWV and the interpolated water vapor density at the center of each layer. The specific formulation is as follows:

$$\begin{aligned} PWV_{GFS}^{cal.} &= PWV_1 + PWV_2 + \cdots + PWV_{L-1} + PWV_L \\ &= \int_{h=h_0}^{h_1} \rho\, dh + \int_{h=h_1}^{h_2} \rho\, dh + \cdots + \int_{h=h_{L-2}}^{h_{L-1}} \rho\, dh + \int_{h=h_{L-1}}^{h_L} \rho\, dh \\ &= \sum_{h=h_0}^{h_1} \rho'_{h_m} \cdot \Delta h + \sum_{h=h_1}^{h_2} \rho'_{h_m} \cdot \Delta h + \cdots + \sum_{h=h_{L-2}}^{h_{L-1}} \rho'_{h_m} \cdot \Delta h + \sum_{h=h_{L-1}}^{h_L} \rho'_{h_m} \cdot \Delta h \end{aligned} \tag{5}$$

where $PWV_1 = PWV_2 = \cdots = PWV_{L-1} = PWV_L = \frac{1}{L} \cdot PWV$,and $h_1, h_2, \cdots, h_{L-2}, h_{L-1}, h_L$ represent the heights of different layers for the key height range of WRF model.

g Derivation of hybrid vertical layering in the WRF model: Following the above steps, the vertical layer heights within the key altitude range for precipitation forecasting in the WRF model can be adaptively determined. By combining these results with the original WRF vertical layers below 1 km and above 7 km, the hybrid vertical layering structure of the WRF model is established, as illustrated in Figure 4.

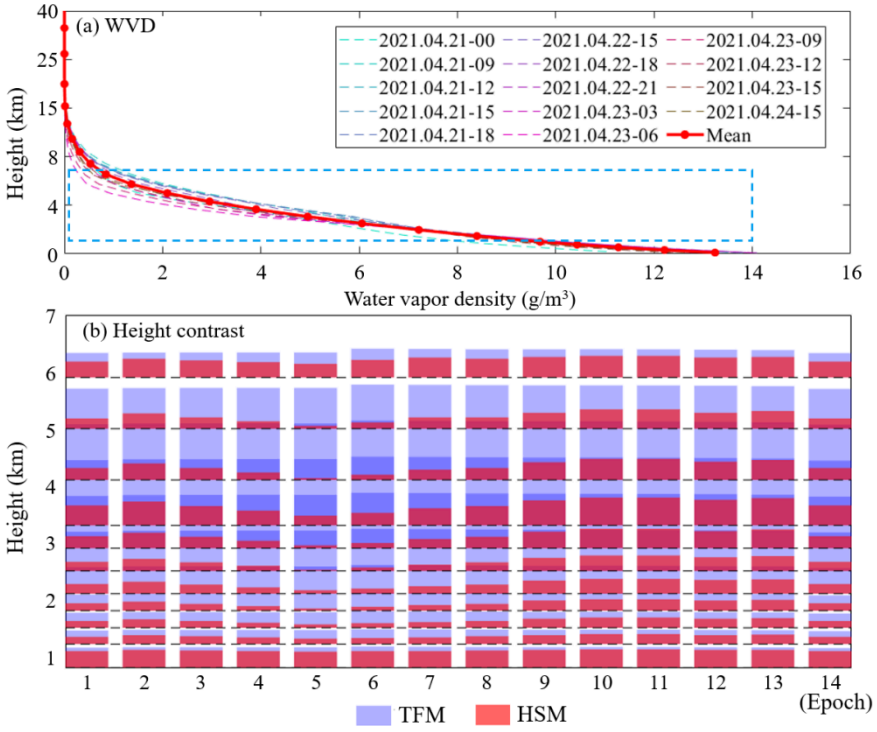

Figure 4. Comparison of water vapor density profiles and vertical layer heights obtained by different methods during the study period: (a) WVD; (b) Height contrast

Figure 4 presents the water vapor density profiles and the corresponding vertical layer heights determined by the proposed method over 14 selected periods. As shown in Figure 4a, the water vapor density profiles exhibit a consistent decreasing trend with increasing altitude. Statistical analysis of the vertical water vapor profiles during the study period indicates that approximately 75%–85% of the total atmospheric water vapor is concentrated below 7 km. This finding is consistent with the general structure of the troposphere, where moisture is primarily distributed in the lower and middle tropospheric layers and plays a dominant role in precipitation formation. Above 7 km, the contribution of water vapor becomes relatively small. While the layer below 1 km is strongly influenced by terrain-following effects and surface processes, making it less suitable for adaptive restructuring without introducing additional uncertainties. Therefore, this study retains the original vertical configuration below 1 km, while focusing on optimizing the layer distribution within the 1–7 km range,

where water vapor gradients are more pronounced and directly related to precipitation processes. It should be noted that the vertical distribution of atmospheric water vapor may vary depending on geographic region and seasonal conditions. Therefore, the selected height range in this study is case-dependent and may require adjustment in different climatic settings.

Figure 4b compares the vertical layer heights obtained using two different stratification methods within the 1–7 km range. The blue–purple lines represent the layer heights derived from the default WRF vertical stratification, while the red lines denote the results obtained using the method proposed in this study. It can be observed that the thickness of each layer increases with altitude, with denser layer distributions in regions of higher water vapor content and sparser distributions in drier regions. In addition, the resulting layer heights vary across different study periods. Given that precipitation is closely associated with the vertical transport of atmospheric water vapor [25], these results indicate that the proposed hybrid stratification method effectively captures the vertical variability of water vapor, thereby providing a more realistic physical basis for short-term precipitation fore-casting.

(2) High-Resolution Land Surface Data Construction

Since the 1990s, with the rapid advancement of urbanization in China, significant changes have occurred in urban morphology, environmental conditions, and socio-economic structures [26]. Driven by economic growth and population expansion, the built-up area of cities has increased substantially [27]. In this context, the default underlying surface data in the WRF model can no longer accurately represent the current land-use conditions in China. Therefore, to address the issues of low quality and outdated default underlying surface data in the WRF model, this study constructs high-quality, high-resolution, and up-to-date land surface data to replace the default dataset.

a Acquisition of underlying surface data: The land-use data used in this study are derived from the Global Land Cover dataset GLC_FCS_30D with a spatial resolution of 30 m for the year 2020. The dataset is available at https://data.casearth.cn/.

b Data preprocessing: ArcGIS is employed to mosaic the acquired raw land-use data, after which the coordinate system of the merged dataset is transformed to the geographic coordinate system WGS_84. Subsequently, the transformed data are reclassified according to the USGS-24 classification scheme used in the WRF model, yielding the reclassified land-use dataset. Table 1 presents the USGS-24 classification system and the corresponding reclassification results

Table 1. Comparison between the USGS-24 classification scheme and the reclassified results of GLC2020.

Land-use category	USGS	GLC2020
Urban and Built-up Land	1	190
Dryland Cropland and Pasture	2	10, 11, 12
Irrigated Cropland and Pasture	3	20
Mixed Dryland/Irrigated Cropland and Pasture	4	20
Cropland/Grassland Mosaic	5	30
Cropland/Woodland Mosaic	6	40
Grassland	7	130
Shrubland	8	120, 121, 122
Mixed Shrubland/Grassland	9	130
Savanna	10	152, 153
Deciduous Broadleaf Forest	11	61, 62
Deciduous Needleleaf Forest	12	81, 82
Evergreen Broadleaf	13	51, 52
Evergreen Needleleaf	14	71, 72
Mixed Forest	15	91, 92
Water Bodies	16	210
Herbaceous Wetland	17	182, 186
Wooden Wetland	18	181, 183, 185
Barren or Sparsely Vegetated	19	150, 152, 153, 184, 187, 200, 201, 202
Herbaceous Tundra	20	140
Wooded Tundra	21	140
Mixed Tundra	22	140
Bare Ground Tundra	23	140
Snow or Ice	24	220

c Data clipping: The reclassified land-use data are clipped according to the spatial extent of the study area to facilitate subsequent format conversion.

d Data format conversion: The static datasets required by the WRF model are stored as binary two- or three-dimensional arrays, which can represent single- or multi-layer continuous or categorical fields. When incorporating a new static dataset, it is necessary to generate both a binary file containing the data and a metadata file ("index") describing the dataset. During the writing process, no file headers, record markers, or additional bytes are included. The data are written row by row from west to east, starting from the southernmost part of the domain. The file naming convention follows the format "xstart-xend.ystart-yend", where xstart, xend, ystart, and yend are five-digit positive integers indicating the starting and ending indices

in the x and y directions, respectively. Subsequently, the name, type, path, and interpolation method of the new dataset are added to the GEOGRID.TBL file, enabling the dataset to be called and interpolated within the WRF preprocessing system. Figure 5 compares the default USGS land-use data used in the WRF model with the updated GLC2020 land-use data. The results show that, with the rapid development in China, urban expansion has accelerated significantly. As illustrated in Figure 5b, urban and built-up areas have increased markedly, accompanied by notable changes in cropland and vegetation types.

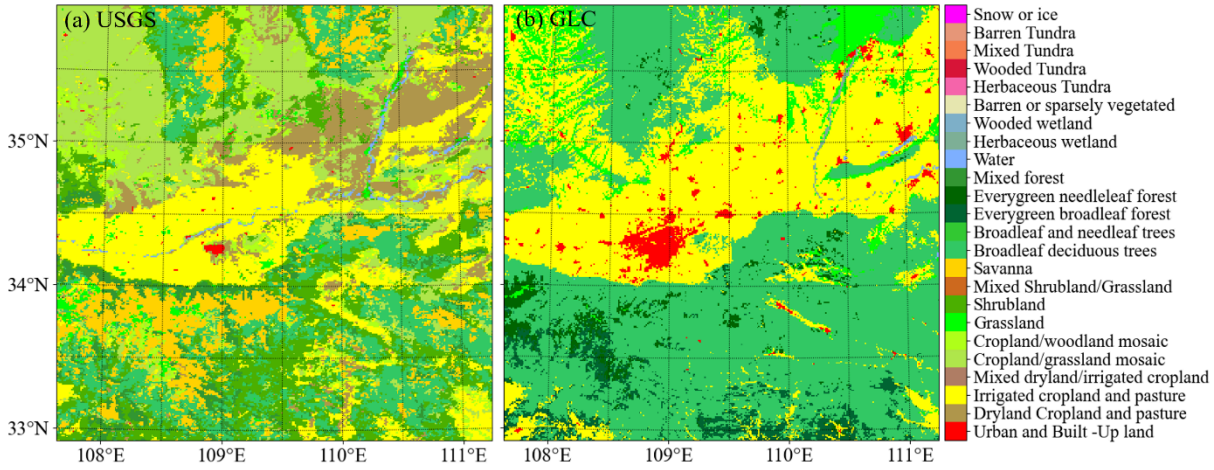

Figure 5. Comparison of USGS and GLC2020 land-use datasets: (a) USGS; (b) GLC

Evaluation Metrics

To evaluate the performance of the model, four statistical metrics—root mean square error (RMSE), Pearson correlation coefficient (R), mean absolute error (MAE), and bias (BIAS)—are employed to assess the accuracy of the meteorological variables. Specifically, RMSE is used to quantify overall prediction accuracy and reflects the reliability of different meteorological parameters; R measures the strength of the linear relationship between simulated and observed values; MAE represents the average magnitude of absolute errors; and BIAS characterizes the systematic deviation of model outputs relative to observations.

$$RMSE = \sqrt{\frac{1}{n}\sum_{i=1}^{n}(x_i - y_i)^2} \tag{6}$$

$$R = \frac{\sum_{i=1}^{n}(x_i - \overline{x})(y_i - \overline{y})^2}{\sqrt{\sum_{i=1}^{n}(x_i - \overline{x})^2}\sqrt{\sum_{i=1}^{n}(y_i - \overline{y})^2}} \tag{7}$$

$$MAE = \frac{1}{n}\sum_{i=1}^{n}|x_i - y_i| \tag{8}$$

$$BIAS = \frac{1}{n}\sum_{i=1}^{n}(x_i - y_i) \tag{9}$$

where x_i denotes the meteorological variable to be evaluated, y_i represents the observed value, and n is the total number of observations.

In addition, categorical verification metrics based on a binary confusion matrix are adopted to evaluate the model's ability to capture precipitation occurrences. These include the probability of detection (POD), false alarm ratio (FAR), miss alarm ratio (MAR), and threat score (TS) [28]. Among them, the TS measures the proportion of correctly predicted precipitation events relative to the total number of observed and/or forecasted events, with values ranging from 0 to 1, where 1 indicates a perfect forecast. A higher TS value corresponds to better precipitation prediction performance, as summarized in Table 2.

Table 2. Reference table for rain/no-rain classification.

Forecast / Observation	rain	no-rain
rain	hits	false alarm
No-rain	misses	-

$$POD = \frac{N_{hits}}{N_{misses} + N_{hits}} \times 100\% \tag{10}$$

$$FAR = \frac{N_{flaseAlarms}}{N_{hits} + N_{flaseAlarms}} \times 100\% \tag{11}$$

$$MAR = \frac{N_{misses}}{N_{hits} + N_{misses}} \times 100\% \tag{12}$$

$$TS = \frac{N_{hits}}{N_{hits} + N_{flaseAlarms} + N_{misses}} \times 100\% \tag{13}$$

where N_{hits} , N_{misses} , and $N_{FalseAlarms}$ denote the number of hits, misses, and false alarms, respectively. The definitions of “hit”, “miss”, and “false alarm” are provided in Table 2 [29].

RESULTS AND DISCUSSION

Scheme design and model configuration

The WRF model in this study employs the high-quality GLC2020 dataset proposed in this work as the underlying surface data. In addition, the selection of physical parameterization schemes is tailored to the climatic characteristics of the study area. Considering that the horizontal resolution of the innermost domain is finer than 3 km, convective processes can be explicitly resolved; therefore, cumulus parameterization is not applied [30]. The main physical parameterization schemes used in the WRF model configuration are summarized in Table 3.

Table 3. Configuration of the WRF model and physical parameterization schemes

Configuration	Domain 1	Domain 2	Domain 3
Projection	Lambert	Lambert	Lambert
Spatial resolution	9 km	3 km	1 km
Temporal resolution	1-h	1-h	1-h
Grid points	112×112	223×223	334×334
Time step	54 s	18 s	6 s
Underlying surface data	GLC2020/USGS		
Model top pressure	50 hPa		
Microphysics scheme	WSM6		
Planetary boundary layer	Yonsei University		
Longwave radiation	RRTMG		
Shortwave radiation	Dudhia		
Surface layer	MM5		
Land surface	Noah LSM		
Cumulus parameterization	Kain-Fritsch	—	

To investigate the impacts of updated land surface data and improved vertical layering on the forecasting performance of the WRF model, four experimental schemes are de-signed in this study. The model outputs are interpolated to the locations of meteorological stations within the study area to evaluate the accuracy of the forecasts under different schemes.

The evaluation focuses on four key meteorological variables: precipitation, temperature, atmospheric pressure, and relative humidity. The detailed configurations of the experimental schemes are summarized in Table 4.

Table 4. Experimental design of WRF model configurations

Scheme	Underlying surface data	Vertical stratification method
1	USGS (default)	TFM (default)
2	GLC2020	TFM (default)
3	USGS (default)	HSM (hybrid vertical stratification)
4	GLC2020	HSM (hybrid vertical stratification)

Evaluation of Precipitation Forecast Performance

To quantitatively assess the performance of precipitation forecasts under different experimental schemes, the WRF-simulated precipitation is compared with observations from meteorological stations within the study area. Figure 6 illustrates the discrepancies between simulated and observed precipitation at an hourly timescale for all four schemes.

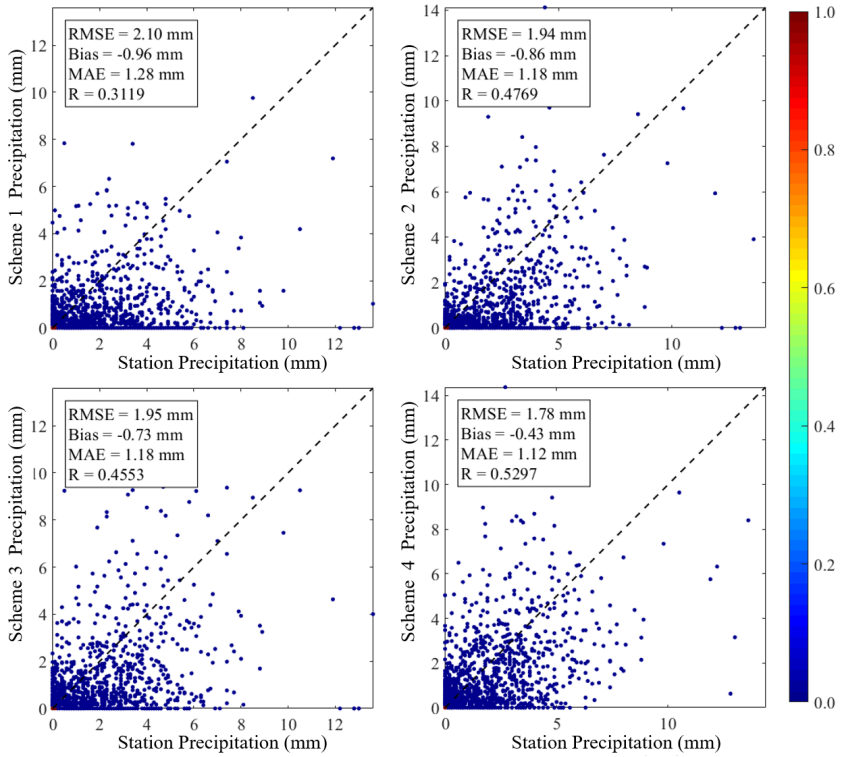

Figure 6. Scatter density plot of hourly precipitation from WRF simulations versus observations at meteorological stations within the study area

The results demonstrate that Scheme 4 consistently outperforms the other configurations, exhibiting the smallest overall deviation and the strongest correlation with observations. Specifically, the mean RMSE, MAE, Bias, and R for Scheme 4 are 1.78 mm, 1.12 mm, −0.43 mm, and 0.53, respectively. Compared with the baseline scheme (Scheme 1), these results correspond to improvements of 15.2% in RMSE, 12.5% in MAE, and 55.2% in Bias, indicating a substantial enhancement in precipitation forecasting accuracy.

In comparison, Schemes 2 and 3—representing the individual contributions of up-dated land surface data and improved vertical layering, respectively—also show noticeable improvements over the baseline. Scheme 2 achieves mean values of RMSE, MAE, Bias, R are 1.94 mm, 1.18 mm, −0.86 mm, and 0.48, while Scheme 3 yields RMSE, MAE, Bias, R are 1.95 mm, 1.18 mm, −0.73 mm, and 0.46. Both schemes outperform Scheme 1 (2.10 mm, 1.28 mm, −0.96 mm, and 0.31), confirming that each individual improvement contributes positively to model performance.

More importantly, the superior performance of Scheme 4 suggests that the combined implementation of high-resolution land surface data and the hybrid vertical layering approach leads to greater improvements than either modification alone. These findings highlight the effectiveness of simultaneously re-fining surface representation and vertical structure in enhancing the WRF model's capability for precipitation forecasting.

To further evaluate the capability of the proposed method in capturing precipitation occurrences, Figure 7 presents the statistical results of the TS, POD, MAR, and FAR for the four experimental schemes.

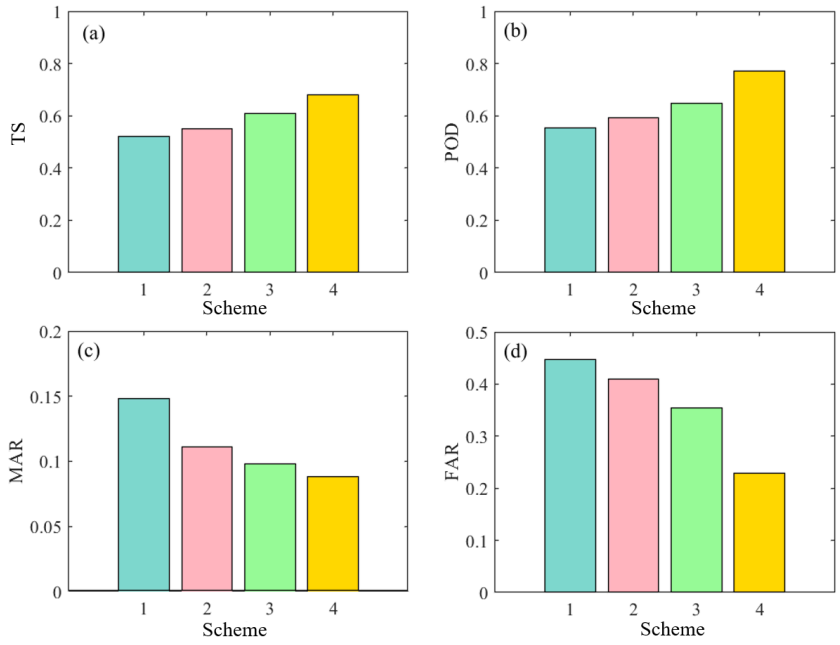

Figure 7. Statistical summary of evaluation metrics for the four WRF experimental schemes compared with station observations

The results indicate that Schemes 2, 3, and 4 all exhibit improvements across the four evaluation metrics compared with the baseline (Scheme 1). Among them, Scheme 4 demonstrates the best overall performance, with mean TS, POD, MAR, and FAR values of 0.68, 0.77, 0.23, and 0.09, respectively. Relative to Scheme 1 (0.52, 0.55, 0.45, and 0.15), these correspond to improvements of 30.7%, 40%, 48.9%, and 40%. The substantial in-crease in TS and POD, together with the marked reduction in MAR and FAR, indicates that Scheme 4 significantly enhances the model's ability to accurately capture precipitation events while effectively reducing both missed detections and false alarms.

Overall, these results demonstrate that updating land surface data and optimizing the vertical layering structure in the WRF model can substantially improve its capability in precipitation event detection and forecasting performance.

To further examine the spatial distribution characteristics of hourly accumulated precipitation under different experimental schemes, observations from 23 national meteorological stations during the period with the most significant precipitation variation were selected. Figure 8 presents the spatial distribution of 1 h accumulated precipitation forecasts at 12:00 on 23 April 2021.

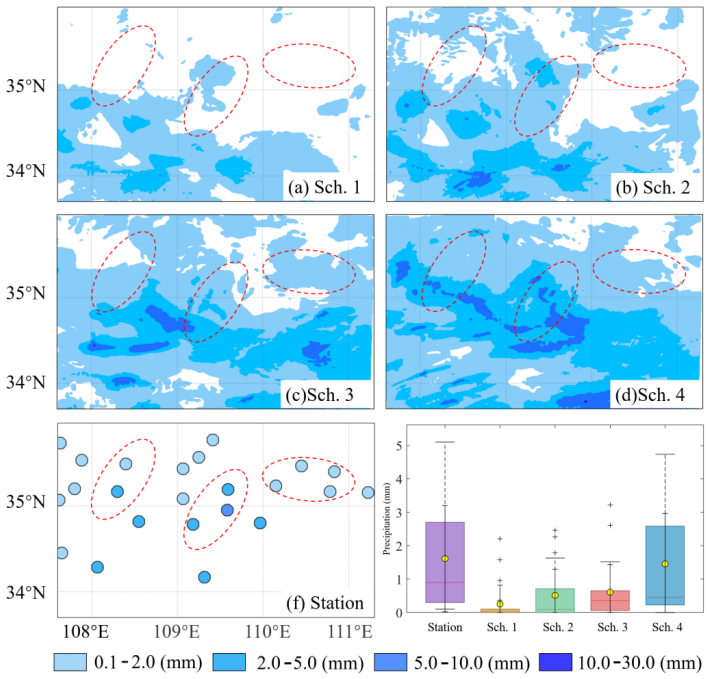

Figure 8. Spatial distribution of 1 h accumulated precipitation forecasts from the four experimental schemes at the time of maximum rainfall variation, along with a comparison with observations from national meteorological stations. Panels (a)–(d) show the spatial distribution of 1 h accumulated precipitation forecasts for the four schemes, and panel (f) presents the spatial distribution of observed precipitation from national meteorological stations

The results reveal that, compared with the baseline scheme, Scheme 4 shows improved agreement with observed precipitation spatial patterns compared to the other schemes, particularly in reproducing the location of major precipitation centres. Although Scheme 4 still shows slight displacement of the heavy precipitation centre, the magnitude of the spatial shift is reduced compared to the other schemes. In contrast, the traditional scheme (Scheme 1) fails to adequately reproduce the spatial pat-tern of hourly accumulated precipitation. Both Scheme 2 (updated land surface data) and Scheme 3 (improved vertical layering) show noticeable improvements in capturing the spatial distribution of precipitation, while their combined implementation in Scheme 4 further enhances the simulated precipitation intensity. In addition, to further quantify the spatial performance, spatial correlation coefficients between simulated and observed precipitation fields were calculated. The spatial correlation coefficients of schemes 1 to 4 are 0.11, 0.44, 0.51 and 0.58 respectively (as shown in Table 5). Scheme 4 exhibits the highest spatial correlation among all schemes, indicating improved spatial consistency with observations.

Table 5. Comparison of R, RMSE, and Bias for the four experimental schemes at the time of maximum precipitation

	R	RMSE	Bias
Scheme 1	0.11	2.09	−1.36
Scheme 2	0.44	1.78	−1.09
Scheme 3	0.51	1.67	−1.01
Scheme 4	0.58	1.39	−0.16

This improvement can be attributed to two key factors. First, the use of high-quality, high-resolution, and up-to-date land surface data provides more accurate initial surface conditions, thereby enhancing the physical realism of land surface processes, boundary layer development, and land–atmosphere interactions in the WRF model. Second, the optimization of the vertical layering structure enables a more realistic representation of the vertical distribution of atmospheric water vapor, which is critical for simulating the evolution of precipitation intensity.

Furthermore, the boxplot analysis indicates that Scheme 4 exhibits smaller discrepancies with observations compared to the other schemes. Overall, these results demonstrate that the combined optimization of land surface data and vertical layering structure significantly improves the WRF model's ability to reproduce both the spatial distribution and intensity of precipitation.

Evaluation of Conventional Meteorological Forecasts

To further assess the performance of the WRF model in simulating near-surface meteorological variables under different experimental schemes, three representative meteorological stations within the study area—Zhashui (57140), Huyi (57132), and Binzhou (57023)—are selected for detailed analysis. These stations are located at elevations of 818.2 m, 411 m, and 919.9 m, respectively, providing a robust basis for evaluating model performance under varying terrain conditions.

Figure 9 illustrates the time series of temperature, atmospheric pressure, and relative humidity at the selected stations during a typical event on 23 April 2021. Overall, all schemes are able to capture the general temporal evolution of the meteorological variables, indicating that the WRF model reproduces the large-scale variation trends reasonably well. However, noticeable differences exist in the degree of agreement with observations.

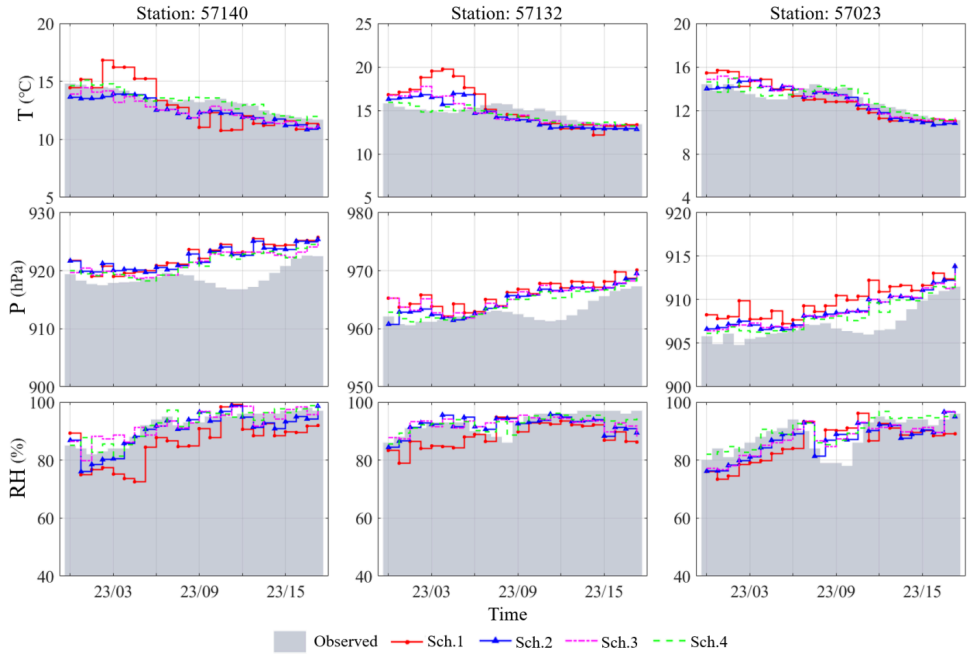

Figure 9. Time series of WRF-simulated temperature, atmospheric pressure, and relative humidity under different experimental schemes, compared with observations at three meteorological stations within the study area.

Among the four schemes, Scheme 4 shows the best overall consistency with observed data, exhibiting smaller deviations across all three stations. In particular, it more accurately captures the amplitude variations and temporal fluctuations of the meteorological variables. In contrast, the baseline scheme (Scheme 1) shows evident biases during certain periods, such as overestimation of temperature and underestimation of relative

humidity. Although Schemes 2 and 3 demonstrate improvements relative to Scheme 1, their performance remains inferior to that of Scheme 4.

These results indicate that the combined optimization of land surface data and vertical layering structure not only enhances forecast accuracy but also improves the model's stability and adaptability under different terrain conditions. Consequently, this integrated approach contributes positively to the WRF model's capability in simulating near-surface meteorological variables.

To further quantify the improvements in forecasting accuracy at the station scale, the root mean RMSE and mean MAE are employed to compare the performance of different experimental schemes in simulating temperature, atmospheric pressure, and relative humidity. Figure 10 presents a radar chart of RMSE and MAE for hourly averaged forecasts of these variables on 23 April 2021.

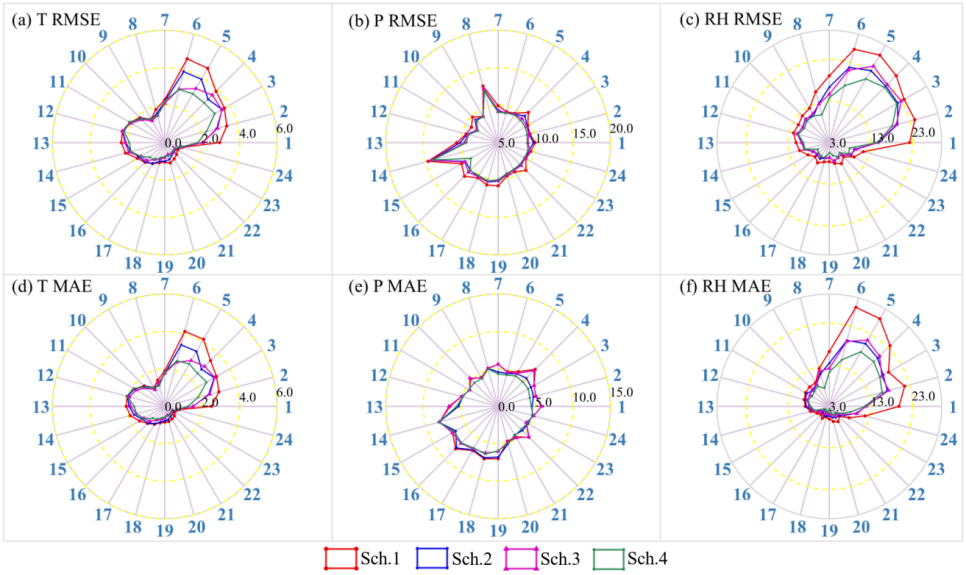

Figure 10. Radar chart of RMSE and MAE for hourly mean forecasts of temperature, atmospheric pressure, and relative humidity under different experimental schemes.

The results indicate that Scheme 4 consistently outperforms the other schemes across most stations, with notable reductions in both RMSE and MAE. Schemes 2 and 3 also show improvements relative to the baseline, but their performance remains inferior to that of Scheme 4. Overall, although the magnitude of improvement for temperature, pressure, and relative humidity is less pronounced than that observed for precipitation forecasts, the proposed approach still demonstrates a clear enhancement over the traditional scheme. This

suggests that the method contributes to improved simulation of short-term near-surface meteorological variables.

Table 6 summarizes the statistical results of the evaluation metrics for the four schemes. For Scheme 4, the RMSE/MAE values for temperature, pressure, and relative humidity are 1.67 °C/1.37 °C, 9.58 hPa/5.12 hPa, and 11.08%/8.86%, respectively. Com-pared with Scheme 1, the corresponding improvements in RMSE/MAE reach 21.2%/25.1% for temperature, 6.6%/12.2% for pressure, and 21.9%/29.7% for relative humidity.

Table 6. Comparative analysis of 1 h forecasts of temperature, relative humidity, and pressure for the four experimental schemes

Metric	Scheme	T℃	P (hPa)	RH (%)
RMSE	1	2.12	10.25	14.20
	2	1.89	9.84	12.09
	3	1.78	9.78	12.06
	4	1.67 (21.2%)	9.58 (6.6%)	11.08 (21.9%)
MAE	1	1.83	5.83	12.24
	2	1.59	5.33	10.17
	3	1.47	5.41	9.95
	4	1.37 (25.1%)	5.12 (12.2%)	8.86 (29.7%)

The consistent reduction in RMSE and MAE demonstrates that the proposed method effectively decreases forecast errors across multiple meteorological variables. These findings further confirm that the combined optimization of land surface data and vertical layering structure significantly enhances the overall performance of the WRF model. It should be noted that this study focuses on improving the representation of vertical water vapor distribution through adaptive layer redistribution. Although key dynamical variables such as vertical velocity and water vapor flux are not explicitly analyzed, the proposed method enhances the resolution of water vapor gradients within the main precipitation layer. Given that vertical moisture gradients are closely linked to convective development and moisture transport, this improvement is is expected to improve the representation of precipitation-related physical processes of precipitation-related physical processes. The observed improvements in precipitation forecasting performance provide indirect support for this mechanism. Further investigation of process-level variables will be conducted in future work.

CONCLUSION

This study proposes a GNSS-PWV-assisted hybrid vertical layering method to im-prove the performance of the WRF model in short-term precipitation forecasting. By integrating high-resolution land surface data with

an optimized vertical layering structure informed by atmospheric water vapor distribution, the proposed approach aims to ad-dress the limitations of conventional WRF configurations. A case study of a precipitation event in Xi'an from 21 to 25 April 2021 is conducted to systematically evaluate the effectiveness of the method. (1) The combined implementation of high-resolution land surface data and hybrid vertical layering (Scheme 4) substantially enhances precipitation forecast accuracy. Compared with the baseline scheme, RMSE, MAE, and Bias are reduced by 15.2%, 12.5%, and 55.2%, respectively, while the correlation coefficient increases to 0.53. Categorical verification metrics further confirm that the proposed method improves the detection capability of precipitation events, with TS and POD significantly increased and MAR and FAR effectively reduced. (2) The proposed method improves the consistency between simulated and observed precipitation in both spatial distribution and intensity. The results demonstrate that the optimized scheme more accurately reproduces the spatial patterns of precipitation, particularly in regions with strong variability. This improvement is attributed to the enhanced physical realism of land–atmosphere interactions and a more accurate representation of the vertical distribution of atmospheric water vapor. (3) In addition to precipitation, the proposed approach also improves the simulation ac-curacy of temperature, atmospheric pressure, and relative humidity. The RMSE and MAE for these variables are consistently reduced across multiple stations and terrain conditions. Although the magnitude of improvement is smaller than that for precipitation, the results demonstrate enhanced model stability and adaptability in simulating near-surface meteorological processes. (4) The results indicate that both updated land surface data and im-proved vertical layering independently contribute to model performance enhancement. More importantly, their combined application leads to greater improvements than either approach applied individually. This highlights the importance of jointly considering surface char-acteristics and atmospheric vertical structure in numerical weather prediction. Although interaction effects are not explicitly tested in this study, the results clearly demonstrate that the combined scheme outperforms the individual configurations.

Overall, the proposed GNSS-PWV-assisted hybrid vertical layering method provides an effective framework for improving the accuracy of high-resolution numerical weather prediction models.

Author Contributions

Conceptualization – Wang R; methodology – Wang R; formal analysis – Wang R; investigation – Wang R; resources – Wang R; writing-original draft preparation – Wang R; writing-review and editing – Wang R;

visualization – Wang R; supervision – Wang R. All authors have read and agreed to the published version of the manuscript.

Conflicts of Interest

The author declares no conflict of interest.

Funding

This research was funded by National Natural Science Foundation of China (Grant NO. 42274039).

Data Sharing Agreement

The datasets used and/or analyzed during the current study are available from the corresponding author on reasonable request.

Acknowledgements

The authors would like to thank the National Centers for Environmental Prediction (NCEP) for providing access to the Global Forecast System (GFS) data. Meteorological Detection Center of China Meteorological Administration (CMA) is also thanked for providing the Global Navigation Satellite System (GNSS)/Met data and hourly data from ground weather stations.

REFERENCES

[1] Wed i NP. Increasing horizontal resolution in numerical weather prediction and climate simulations: Illusion or panacea? Philosophical Transactions of the Royal Society A. 2014;372:20130289. doi: 10.1098/rsta.2013.0289

[2] Castorrini A, Gentile S, Geraldi E, Bonfiglioli A. Increasing spatial resolution of wind resource prediction using NWP and RANS simulation. Journal of Wind Engineering and Industrial Aerodynamics. 2021;210:104499. doi: 10.1016/j.jweia.2021.104499

[3] Das S. Challenges in predicting extreme weather events over the South Asian region. In: Extreme Natural Events: Sustainable Solutions for Developing Countries. 2nd ed. Singapore: Springer Nature; 2022. p. 51–106. doi: 10.1007/978-981-16-4812-5_3

[4] Chawla I, Osuri KK, Mujumdar PP, Niyogi D. Assessment of the Weather Research and Forecasting (WRF) model for simulation of extreme rainfall events in the upper Ganga Basin. Hydrology and Earth System Sciences. 2018;22:1095–1117. doi: 10.5194/hess-22-1095-2018

[5] Fox-Rabinovitz MS, Lindzen RS. Numerical experiments on consistent horizontal and vertical resolution for atmospheric models and observing systems. Monthly Weather Review. 1993;121:264–271. doi: 10.1175/1520-0493(1993)1212.0.CO;2

[6] Persson POG, Warner TT. Model generation of spurious gravity waves due to inconsistency of the vertical and horizontal resolution. Monthly Weather Review. 1991;119:917–935. doi: 10.1175/1520-0493(1991)1192.0.CO;2

[7] Xu DS, Liang J, Lu Z, Zhang Y, Huang F, Feng Y, Zhang B. Improved tropical cyclone forecasts with increased vertical resolution in the TRAMS model. Journal of Tropical Meteorology. 2022;28:377–387. doi: 10.46267/j.1006-8775.2022.028

[8] Yang Y, Gao S. Sensitivity study of vertical resolution in WRF numerical simulation for sea fog over the Yellow Sea. Acta Meteorologica Sinica. 2016;74:974–988. doi: 10.1007/s13351-016-6011-1

[9] Khansalari S, Ranjbar-Saadatabadi A, Fazel-Rastgar F, Raziei T. Synoptic and dynamic analysis of a flash flood-inducing heavy rainfall event in arid and semi-arid central-northern Iran and its simulation using the WRF model. Dynamics of Atmospheres and Oceans. 2021;93:101198. doi: 10.1016/j.dynatmoce.2021.101198

[10] Yin JF, Wang DH, Liang ZM, Liu CJ, Zhai GQ, Wang H. Numerical study of the role of microphysical latent heating and surface heat fluxes in a severe precipitation event in the warm sector over southern China. Asia-Pacific Journal of Atmospheric Sciences. 2018;54:77–90. doi: 10.1007/s13143-017-0052-1

[11] Wu Z, Jiang C, Deng B, Chen J, Liu X. Sensitivity of WRF simulated typhoon track and intensity over the South China Sea to horizontal and vertical resolutions. Acta Oceanologica Sinica. 2019;38:74–83. doi: 10.1007/s13131-019-1393-4

[12] Shao M, Zhang Y, Xu JJ. Impact of vertical resolution, model top and data assimilation on weather forecasting: A case study. Journal of Tropical Meteorology. 2020;26:71–81. doi: 10.16555/j.1006-8775.2020.007

[13] López-Espinoza ED, Zavala-Hidalgo J, Mahmood R, Gómez-Ramos O. Assessing the impact of land use and land cover data representation on weather forecast quality: A case study in central Mexico. Atmosphere. 2020;11:1242. doi: 10.3390/atmos11111242

[14] Karakani EG, Mohammadi H, Azizi G, Shamsipour V, Fattahi E. Temperature simulation by numerical modeling and feedback of geostatic data and horizontal domain resolution. Modeling Earth Systems and Environment. 2024;10:3845–3864. doi: 10.1007/s40808-023-01852-0

[15] Jee JB, Kim S. Sensitivity study on high-resolution numerical modeling of static topographic data. Atmosphere. 2016;7:86. doi: 10.3390/atmos7070086

[16] Yan Y, Tang J, Wang S, Niu X, Wang L. Uncertainty of land surface model and land use data on WRF model simulations over China. Climate Dynamics. 2021;57:1833–1851. doi: 10.1007/s00382-021-05763-2

[17] Schicker I, Arnold Arias D, Seibert P. Influences of updated land-use datasets on WRF simulations for two Austrian regions. Meteorology and Atmospheric Physics. 2016;128:279–301. doi: 10.1007/s00703-015-0408-7

[18] Zhang X, Liu L, Chen X, Gao Y, Xie S, Mi J. GLC_FCS30: Global land-cover product with fine classification system at 30 m using time-series Landsat imagery. Earth System Science Data. 2021;13:2753–2776. doi: 10.5194/essd-13-2753-2021

[19] Müller M, Kašpar M, Řezáčová D, Sokol Z. Extremeness of meteorological variables as an indicator of extreme precipitation events. Atmospheric Research. 2009;92:308–317. doi: 10.1016/j.atmosres.2008.10.007

[20] Halperin DJ, Penny AB, Hart RE. A comparison of tropical cyclone genesis forecast verification from three Global Forecast System (GFS) operational configurations. Weather and Forecasting. 2020;35:1801–1815. doi: 10.1175/WAF-D-19-0235.1

[21] Forbis D. Accuracy and variability analysis of the Global Forecast System's near-surface temperatures throughout the contiguous United States [dissertation]. Macomb, IL, USA: Western Illinois University; 2021.

[22] Zhang H, Li H, Fan S. Indicators for the compression and stretching characteristics of the HTF-coordinate of WRF. Advances in Meteorology. 2020;2020:8854761. doi: 10.1155/2020/8854761

[23] Daniels MH, Lundquist KA, Mirocha JD, Wiersema DJ, Chow FK. A new vertical grid nesting capability in the Weather Research and Forecasting (WRF) model. Monthly Weather Review. 2016;144:3725–3747. doi: 10.1175/MWR-D-16-0047.1

[24] Beck J, Brown J, Dudhia J, Gill D, Hertneky T, Klemp J, Wang W, Williams C, Hu M, James E, Kenyon J, Smirnova T, Kim J. An evaluation of a hybrid, terrain-following vertical coordinate in the WRF-based RAP and HRRR models. Weather and Forecasting. 2020;35:1081–1096. doi: 10.1175/WAF-D-19-0145.1

[25] Chen X, Lou Y, Zhang W, Dosa J, Zhou L, Zhou Y. A case study of the "21.7" Henan extremely rainfall event: From the perspective of water vapor monitored with GNSS tomography. Advances in Space Research. 2025;75:1719–1731. doi: 10.1016/j.asr.2024.11.012

[26] Wei YD, Ye X. Urbanization, urban land expansion and environmental change in China. Stochastic Environmental Research and Risk Assessment. 2014;28:757–765. doi: 10.1007/s00477-013-0782-0

[27] Wang X, Shi R, Zhou Y. Dynamics of urban sprawl and sustainable development in China. Socio-Economic Planning Sciences. 2020;70:100736. doi: 10.1016/j.seps.2019.100736

[28] Li H, Wang X, Choy S, Jiang C, Wu S, Zhang J, Qiu C, Zhou K, Li L, Fu E, Zhang K. Detecting heavy rainfall using anomaly-based percentile thresholds of predictors derived from GNSS-PWV. Atmospheric Research. 2022;265:105912. doi: 10.1016/j.atmosres.2021.105912

[29] Wilks DS. Statistical Methods in the Atmospheric Sciences. Cambridge, MA, USA: Academic Press; 2011. doi: 10.1016/C2009-0-00020-6

[30] Guo H, Ma Y, Li Z, Zhao Q, Zhai Y. The evaluation of rainfall forecasting in a global navigation satellite system-assisted numerical weather prediction model. Atmosphere. 2024;15:992. doi: 10.3390/atmos15080992